Combustion of Flat Shaped Char Particles With Oxygen

Henry J. Molintas
Department of Mechanical Engineering,
University of Maryland,
College Park, MD 20742
e-mail: molintas@umd.edu

Ashwani K. Gupta
Distinguished University Professor
Department of Mechanical Engineering,
University of Maryland,
College Park, MD 20742
e-mail: akgupta@umd.edu

Thin flat-shaped carbon black particles of 1.5 mm thickness by 22.5 mm diameter were combusted in pure oxygen at atmospheric pressures and temperatures in the range of 500–650 °C. One-film kinetic-diffusion model was derived to characterize the kinetic and energy parameters for particles arranged in the form of a thin flat-shaped configuration. The kinetic and energy parameters, and operating regimes of thin flat-shaped char particles were characterized during the nonisothermal combustion process. The gasification regimes during preheating were also analyzed. Steady-state energy processes were considered to derive an energy conservation equation used for calculating the evolution of char surface temperatures as well as released peak energy rates and the specific energy, which are considered key engineering design parameters. The one-film kinetic-diffusion model showed that combustion of such particles was purely kinetic controlled under these conditions. The activation energy obtained varied between 50 and 74 kJ/mol using discrete time and linear fits to the Arrhenius equation. The total energies released per weight of char converted varied between 32.8 and 40.6 kJ/g. The highest peak energy rate released was 134 J/s when combusting char in O_2 at a reactor temperature of 504 °C.
[DOI: 10.1115/1.4050907]

Keywords: air emissions from fossil fuel combustion, energy conversion/systems, energy extraction of energy from its natural resource, energy systems analysis, fuel combustion

1 Introduction

The utilization of large particles as feed stock for combustors and gasifiers is important as they offer potential for small-scale, compact, and transportable systems from their greatly reduced preprocessing. Additionally, such systems can easily be deployed, which makes them attractive for isolated, space-limited, and remote area applications. Most of these areas have abundant biomass-based fuels in the form of biodegradable solid wastes such as wood, paper, and cardboard. Biomass-based fuels are increasingly attractive because of their carbon neutral advantages over conventional fossil fuels. As a result, research in these areas has been active and grown in recent years [1–5]. For direct combustion of biomass, air flame and laminar burning speed were measured to provide design rules for combustors [6]. Nonetheless, greater scientific understanding for the processing of large size char particles is still needed to develop efficient small-scale biomass-based energy conversion as applied to gasification systems. Gasification of biomass is considered to be more attractive than biomass combustion because of the potential increase in improving energy conversion. But this approach requires the need to under the conversion of char particles because such materials control most of the process. Key gasifier engineering design requirements such as energy parameters (e.g., thermal efficiency, peak energy rates, and energy value of feedstock) and kinetic parameters (KPs) are not fully known for more realistic nonisothermal operation of gasifiers. The energy parameters could vary, depending on reactor temperature and feedstock conditions [7]. Process kinetic parameters to predict burning rates also remain unknown, especially for large char particles with diameters and thicknesses greater than 1 mm when diffusion rates are expected to influence the overall reduction or conversion process [8–10]. Currently, most studies on coal particles provide conversion rates and kinetic parameters with some reasonable accuracy for small size particles (<0.15 mm) when combusted or gasified isothermally and nonisothermally [11–15]. These studies were generally focused on utilizing pulverized coal as energy resource because of abundant coal availability. Also, coal fired power plants are logistically installed near high energy load demand areas to reduce electrical energy transmission losses. Very few studies are available especially for large size particles that also operate under nonisothermal conditions. In the absence of design guidelines, particularly on the energy and kinetic parameters for the combustion and gasification of large char particles, energy conversion systems are usually designed using trial and error approaches. These approaches can result in undersized/oversized, unstable, expensive and inefficient system. The heating value of solid fuels, reactor thermal efficiency, and the rate of energy released during combustion of solid fuels are also important design considerations to properly size combustors or gasifiers. Determination of such energy parameters allows designers to evaluate the thermochemical conversion systems for optimized operation.

Combustion of solid fuels in air generally requires large exhaust systems due to the presence of nitrogen gas in air, especially when excess air is used to improve conversion. However, use of pure oxygen or when mixed with air or steam as oxidant, enhances the thermal efficiency and carbon conversion to result in a compact thermochemical processor. Oxy-combustion of biomass, either in the raw or torrefied state also has shown a high combustion effectiveness, resulting to low CO and SO_2 [16]. Compact processors are attractive for space constrained environments (e.g., navy, and cargo ships, urban and remote areas as well extra-terrestrial applications). Compact processors also provide advanced applications for waste-to-energy or biomass energy conversion systems. For land or sea-based systems, the use of recycled or recovered hot vitiated air (products of combustion from diesel engines or gas turbines) offers advantages for improving thermal efficiency.

This study examines the reduction of char particles initially of 1.5 mm thick and up to 22.5 mm in diameter using pure O_2 and hot vitiated air. The formulation of some basic equations is presented to help support the development of suitable analytical tools. These tools enable the calculations of time-dependent energy rates by using Euler Explicit Method via discrete nonlinear fit (DNLF) and direct linear fit to obtain kinetic parameters. This numerical method is also investigated to characterize the operating

Contributed by the Advanced Energy Systems Division of ASME for publication in the Journal of Energy Resources Technology. Manuscript received April 2, 2021; final manuscript received April 14, 2021; published online May 19, 2021. Editor: Hameed Metghalchi.

regimes and the relationships of these parameters with the burning rates. The time-dependent char surface temperatures were evaluated with the numerical method by considering the temporal variations in observed weight and particle diameter every 20 s. Observed weight loss was optimized to follow an exponential trend via the use of nonlinear regression to reduce the noise measured during experimental data acquisition. Additionally, these optimized measured weight losses were fitted into the equations to determine the regime of reduction as well as the kinetic parameters, starting from the preheating stage up to the end of the combustion process when most of the char particles reached complete conversion. With this approach, the kinetic parameters, operating regimes and energy parameters (e.g., thermal efficiency, peak energy rates, and specific energy released) of thin flat disk-shaped char particles during combustion were characterized using the one-film burning model. Blackbody radiation and steady-state energy processes for the one-film model were also considered to calculate the energy parameters. Nonisothermal conditions were used to simulate the operation of real-world combustors and gasifiers. Our objectives for the operating conditions of 4 m^3/h O_2 flowrate at 1 atm. were to determine:

(a) Effect of different injection temperatures on complete char conversion for 0.2 g samples.
(b) Effect of different injection temperatures on calculated char surface temperatures.
(c) Effect of air and partial CO_2 gasification models on the preheat gasification stages from 100 °C up to the specified injection temperatures.
(d) Effect of char surface temperatures on the kinetic parameters.
(e) Peak energy rates, specific energy value, and thermal efficiency.

2 Heterogeneous Reactions

The combustion and gasification of solid fuels were considered heterogeneous reactions, wherein the reactants exist in both solid and gaseous states. These reactions consider some or all of the following [17]:

(a) Transport of the reactant molecule (e.g., O_2, air, H_2O, or CO_2) to the solid surface occurs either by convection and/or diffusion.
(b) Adsorption of the reactant molecule occurs on the solid surface.
(c) Elementary reaction steps involve various combinations of adsorbed molecules, the solid surface, and gas-phase molecules.
(d) Desorption of product molecules from the solid surface.
(e) Transport of the product molecules away from the surface occurs by convection and/or diffusion.

Among these processes, (a) and (e) can be analyzed using mass transfer concepts. The intervening steps are more complex, especially step (c). Step process (b) can be analyzed depending on how strongly or weakly the reactant gas molecules are adsorbed to the solid surface. For a single gas molecule reactant (oxygen), the global reaction rate (R_c) with a unity order of reaction for an oxygen molecule that is weakly adsorbed to the surface can be expressed as [18]

$$R_C = \dot{m}''_{C,s} = k_c MW_C [O_{2,s}] \tag{1}$$

where $[O_{2,s}]$ is the molar concentration of O_2 at the surface and k_c is the rate coefficient of reaction, expressed in Arrhenius form. When the oxygen molecule is strongly adsorbed at the solid surface, the reaction rate becomes independent of the gas-phase concentration of oxygen as [18]

$$R_C = \dot{m}''_{C,s} = k_c MW_C \tag{2}$$

Both Eqs. (1) and (2) assume a global reaction rate of unity order of reaction at the solid surface. This can be further classified into three reduction scenarios of (a) one-film, (b) two-film model, and (c) continuous-film [18]. The one-film model assumes that there is no flame in the gas phase and the maximum temperature occurs at the solid surfaces. For the two-film model, a flame exists in the gas phase at some distance from the solid surface wherein the intermediate species (e.g., CO) reacts with the incoming reactants (O_2). A continuous-film model assumes a distributed flame zone within the boundary layer [18].

Among these three models, the one-film is simplest and hence pursued further here to characterize the kinetic parameters, evolution of char surface temperatures, contribution of diffusional effects, and various energy parameters during char combustion for known fuel burning rates. A thin flat-shaped char particle was considered here using the following assumptions in the one-film diffusion-kinetic model [19]:

- The solid carbon surface burns in quiescent medium such that the effects of convection are ignored. This can be assumed because of very small velocity (i.e., 0.1 m/s) at the solid surface.
- At the particle surface, carbon char reacts kinetically with reactant molecule (O_2 or CO_2).
- The reactant molecules (O_2 or CO_2) are weakly adsorbed on the char surface, which means that the $d[\text{Char}]/dt = k(T)[O_2]$ or $[\text{Char}]/dt = k(T)[CO_2]$ governs during combustion or gasification, respectively.
- The gas phase consists of only O_2 and CO_2 for combustion conditions. The O_2 diffuses inward and reacts with the carbon surface to form CO_2 gas which diffuses outward.
- The gas phase consists of only CO_2 and CO for gasification conditions. The CO_2 diffuses inward and reacts with the carbon surface to form CO gas, which diffuses outward.
- The carbon internal surface is impervious to gas species and intra-particle gas diffusion is ignored. This is made possible by using a thin layer of char particles.
- The carbon surface temperatures are calculated based on blackbody radiation, steady-state process, and no heat conduction into the particle interior.

Although the measured or observed weights and particle diameters changed sometimes erratically due to experimental noises, these were optimized with nonlinear regression on the experimental data to provide stable calculation of surface temperatures, which were then used to calculate the kinetic parameters.

3 Analytical Approach

3.1 One-Film Equation. Using the above assumptions, the mass loss rate from the one-film kinetic-diffusion equation using a flat thin layer and disk-shaped char configuration was derived and is given by

$$\frac{dm}{dt} = \frac{Y_{O_2,\infty}}{\dfrac{H(\nu_I + Y_{O_2,s})}{\rho D \pi r^2} + \dfrac{MW_{O_2} \times R_u T_s}{\pi r^2 k_c MW_c \times P \times MW_{mix}}} \tag{3}$$

where dm/dt is the derivative of mass loss with respect to t, r is instantaneous equivalent radius of the char in the container, $Y_{O2,s}$ is the mass fraction of O_2 at the surface of the char, $Y_{O2,\infty}$ is the mass fraction of O_2 at the far field, D is the mass diffusivity of reactant and product gases in the reaction, H is the height of the stagnant layer, ν_I is the stoichiometric coefficient (2.667 for combustion and 1.333 for air gasification), k_c is the rate coefficient, and MW are the molecular weight of the species of interest. Equation (3) is a one-dimensional (1D) equation, coupling both the external diffusion effects and kinetics for gasification or combustion of thin flat-shaped char particles. This equation provides the physical characteristics of the experiments performed for thin char layers with some idealizations, see Fig. 1. The rate of mass loss due to diffusion effects and kinetics for thin layer or disk-shaped char particles are underscored by considering constant values of the stagnant layer (H) and char thickness (h). The particle radius (r) was also allowed to change due to reduction condition by considering

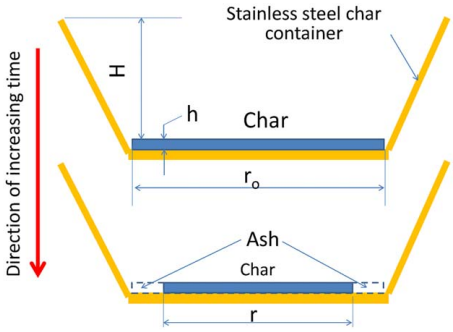

Fig. 1 Expose thin flat-shaped disk model

constant char density of 0.335 g/c m^3. Kinetic calculation procedure involved solving for the rate coefficient (k_c) in Eq. (3). Then, the activation energies and frequency factors were calculated by fitting the observed and experimental values in this equation until the weight curve model approximated the experimental values at specific times. The changes in apparent activation energies, surface char temperatures, and resistances of the external chemical reaction and diffusion rates were calculated with Euler Explicit Method for each particle case investigated at every 20 s intervals. This numerical method allowed us to iteratively calculate the rate coefficients with respect to temporal variation of char conversion. When the weight loss model finally converged to follow the optimized experimental data curve via nonlinear regression, discrete time linear method was used for the Arrhenius equation to estimate the activation energies and frequency factors. Suitable discrete time intervals were assigned to obtain logarithmic plot of rate coefficients as a function of reciprocal of temperatures. Using electrical current flow analogy, the expressions in the denominators of Eq. (3) can be categorized explicitly as two resistances given by Eqs. (4) and (5)

$$R_{diff} = \frac{(v_I + Y_{O_2,s})H}{\rho D \pi r^2} \tag{4}$$

$$R_{kin} = \frac{MW_{O_2} \times R_u T_s}{\pi \times r^2 k_c MW_C \times P \times MW_{mix}} \tag{5}$$

The rate coefficient of reaction expression or the Arrhenius equation is shown in Eq. (6)

$$k_c = A \times \exp\left(-\frac{E_a}{RT_s}\right) \tag{6}$$

The rate coefficient (k_c) was calculated by fitting the experimental data into Eq. (3). In Eq. (3), a unity order of reaction was used to simplify the analysis. Using natural logarithms in Eq. (6), the values of E_a and A can be directly calculated. Under pure diffusion-controlled conditions, R_{kin} is equal to zero and conversely, for a pure (intrinsic) kinetic-controlled conditions, R_{diff} is equal to zero. The ratio of R_{kin} to R_{diff} provides a convenient way of indicating when the reduction is externally diffusion-controlled, intermediate or externally kinetically controlled, i.e., $R_{kin}/R_{diff} \ll 1$, $R_{kin}/R_{diff} = 1$, and $R_{kin}/R_{diff} >> 1$, respectively [18].

The reduction of char radius (r) was modeled with respect to time using Eq. (3). In the experiments, char particle radius was observed to decrease with increase in reaction progress. This char radius does not directly represent the actual radius of the flat-shaped arranged particles but rather the equivalent size reduction as the char shrinks during oxidation. Figure 1 illustrates this with the assumption that the thickness of the char (h) remains constant. Starting with the basic formula for mass with respect to density and volume, the char mass can be expressed as follows:

$$m = \rho_c \times v \tag{7}$$

Substituting the volume with respect to char radius and depth, the mass of char can be expressed as

$$m = \rho_c \times \pi r^2 h \tag{8}$$

Differentiating Eq. (8) with respect to time yields

$$\frac{dm}{dt} = \rho_c \times 2\pi r h \frac{dr}{dt} \tag{9}$$

Knowing the values of dm/dt, the changes in char radius with respect to time can be calculated as

$$\frac{dr}{dt} = \frac{1}{2\pi r \rho_C h} \times \frac{dm}{dt} \tag{10}$$

where, dr/dt is the instantaneous rate of change of radius, r is the char radius at time t, ρ_c is the char's bulk density as measured, and dm/dt is the instantaneous experimental rate of char mass. Depending on the region of the reactions, dm/dt and r are constantly changing and are expected to change significantly when char reactions occur very fast. The experimental values of dm/dt are fitted into Eq. (10) to calculate dr/dt.

Equation (3) was used to fit different values of rate coefficients until the mass loss model fitted the experimental mass loss values. The succeeding mass loss model values were then calculated using Euler Explicit Method at every 20 s intervals. Through iterations and trial values of the rate coefficient (kc), model weight loss values were obtained until a good fit to the optimized experimental weight loss curve was observed. Equation (3) reveals that under pure diffusion-controlled conditions, the activation energy is irrelevant. Two chemical pathway mechanisms during diffusion-controlled reactions can be determined. For $C + 1/2O_2 \rightarrow CO$ and $C + O_2 \rightarrow CO_2$, the stoichiometric coefficients are 1.333 and 2.667, respectively. At the start of determining the regimes during the preheat periods, which begins at 100 °C, the model was adjusted to follow for any of the above two mechanisms by adjusting the values of the stoichiometric coefficients. The model that best fitted the experimental values provided the regime of char reduction process. Although internal reactions can also occur during char oxidation periods, these were assumed negligible because the char particles were thinly distributed in the container and the diffusing gases can effectively travel only at the external surfaces of the char.

3.2 Energy Conservation Equation for the One-Film Model. The char surface temperatures (T_s) were calculated iteratively by considering a blackbody radiation, steady-state process and negligible heat conduction into the particle interior. The time evolution of char surface temperatures were calculated based on + or –1% of the total energy released during combustion. Distibuted energy loss during combustion was mainly due to radiation. The energy loss due to conduction was very small. For this case, the energy flows at the particle surface and mass transfer effects on energy were coupled together to allow for a derivation of the governing equations for flat char discs. The resulting equations incorporate the energies that are released from the char surface via heat from radiation and gas-phase mass transfer. The gas-phase thermal conductivities and specific heats of the oxidants (e.g., O_2, air, and CO_2) under consideration were varied based on the calculated char surface temperatures. Varying Lennard-Jones parameters with changes in temperature were also used to calculate the diffusion coefficients of prevailing gases produced from these reactions [18,19]. The gas-phase reactions taking place at the boundary layer (i.e., two-film) of these particles were neglected for mathematical expediency. Also, for these particles, most of the CO produced were combusted very close to the char disc surface where the combustion occurred. Based on this simplification, the derived Eq. (11) can be used to calculate thin flat-shaped char surface temperatures

$$\dot{m}_C \Delta h_C = H \times \rho C_p D(T_S - T_\infty) + \varepsilon_S \pi r^2 \sigma (T_S^4 - T_\infty^4) \tag{11}$$

Table 1 Physical properties of commercial carbon black [20]

BET surface area (m^2/g)	Total pore volume (ml/g)	Percentage of mesopores by weight (2 nm < pore dia. 50 nm)	Percentage of macropores by weight (pore dia. > 50 nm)	Percentage of micropores by weight (pore dia. < 2 nm)	Particle size per SEM	Density (g/cm^3)
29.8	0.047	77.6	22.1	1.3	~6 μm	1.3–1.7

Equation (11) assumes that the energy loss due to transport by convection was negligible and that no energy was released due to chemical reaction in the gas phase under steady-state conditions. Based on the one-film model, this implies that the desorbed CO gas was instantaneously converted to CO_2 gas very close to the external surface of char particles.

For the gasification of flat char particles, the first term on the right-hand side of Eq. (11) was neglected because of small convection term, leaving behind only the radiation term. However, the temperature terms (T_s and T_∞) were switched because the reactor radiates to the char surface during gasification.

System thermal efficiencies were calculated for each case of combustion and gasification of char particles. Efficiencies for combustion condition included the input energy required to compress air from atmospheric conditions to 101.325 atm and the combustion of propane gas.

4 Experimental

4.1 Materials for Char. Commercial lamp black (also called oil black; Fisher, CAS 1333-86-4, catalog no. C198-500) was used as the model material to form flat thin layer char particles in the form of a disc. This lamp black material was manufactured from oil with extreme heat without using any solvent. This material was chosen because of its relatively well-defined characteristics with less than 0.1% tar content and has a total polycyclic aromatic hydrocarbons (PAHs) concentration of about 700 ppm. Properties of the lamp black are given in Table 1 [20].

The specific density was between 1.3 and 1.7 g/cm^3 and BET surface area (measured by N_2 adsorption) was similar to the calculated exterior surface area of 18–23 m^2/g for spherical particles [21]. A single collection of particles as used in the experiments had a bulk density of about 0.335 g/cm^3. Average sample weight was 0.2 g. The average thickness and radius were 1.52 and 11.26 mm, respectively. This represents 82.8% porosity based on the density of pure carbon of 1950 g/cm^3 [22]. Figure 2 shows that carbon black particles tend to approximate a spherical shape. This image reveals that Fisher lamp black structure was compact so that the pores were too small for reactant gases. This figure further reveals the effects of van Der Waal forces between the particles, enabling these to be actually heavier than a single particle (which was also supported from the calculated lift, drag, and anchoring forces).

Figure 3(*a*) depicts a typical single particle resting on a surface. Particles in this configuration experience a lift force perpendicular to the direction flow of oxidants. This lift force can be calculated using Eq. (12) assuming that the particles are nearly spherical in shape [23]

$$F_L = \frac{0.58\rho_g u^4 (d_p)^4}{v^2} \tag{12}$$

where F_L, ρ_g, u, d_p, and v represent the lift force, oxidant density, oxidant velocity, particle diameter, and oxidant kinematic viscosity, respectively. The Reynolds number of a single particle was 5.83×10^{-5} based on 0.1 m/s gas velocity and 0.06 μm particle diameter. And for a very low Re, the drag force for a spherical particle was estimated using Eq. (13) [24]

$$F_D = 8\frac{(\rho d_p u)^2}{\rho\left\{1 + K_n\left[1.257 + 0.4\exp\left(\frac{-1.1}{K_n}\right)\right]\right\}} \tag{13}$$

where F_D, u, d_p, ρ, and K_n represent the drag force, oxidant velocity, particle diameter, density, and Knudsen number, respectively. The required anchoring force was estimated with Eq. (14) using a coefficient of friction of 0.14 between carbon and steel surfaces [24]

$$F_A = \sqrt{W_\rho^2 + [0.14(W_p - F_L)]^2} \tag{14}$$

where F_A and W_p represent the anchoring force, and particle weight, respectively. The normal force is the difference between the particle

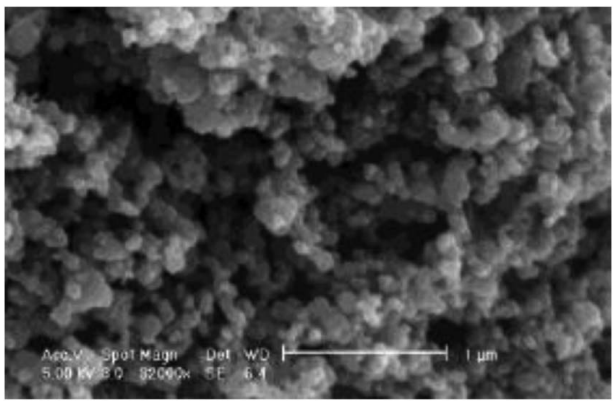

Fig. 2 Scanning electron microscopy (SEM) images of Fisher lamp black [21]

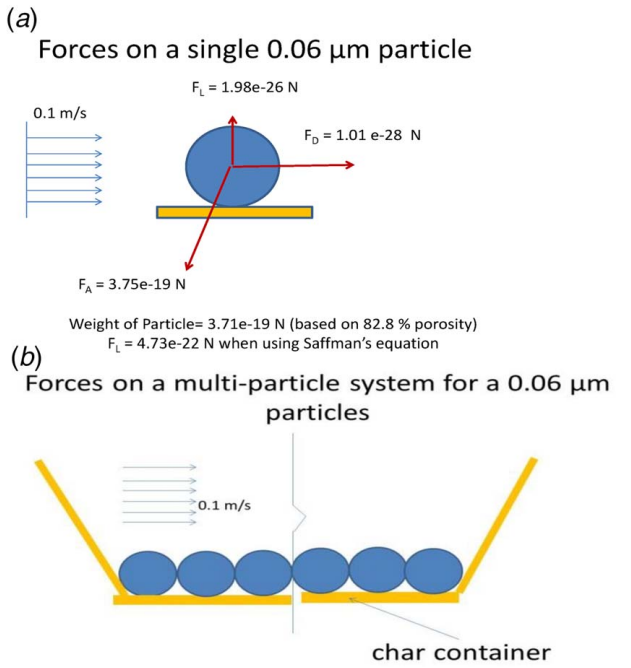

Fig. 3 (*a*) Forces on a single particle char and (*b*) forces acting on layered multiple particles

weight and lift force, F_L. When these equations are evaluated based on particle diameter of 0.06 μm, they provided lift and drag forces equal to 1.98×10^{-26} (note that Saffman's equation provides $F_L = 4.73 \times 10^{-22}$ N (newton) when particle was in suspension and not anchored) and 1.01×10^{-28} N, respectively (see Fig. 3(*a*)). Because the particle weight at 3.71×10^{-19} N (based on 82.8% porosity) is greater than the lift force, it was expected that the particle cannot be lifted up, assuming no anchoring forces due to molecular forces. The drag force at 1.01×10^{-28} N is also lower than the maximum possible anchoring force (F_A) at 3.75×10^{-19} N for a single particle, which implies that the particle cannot roll or get entrained in the oxidant gas stream. Nonetheless, for a multi-particle system as shown in Fig. 3(*b*), the resulting drag and lift forces were also constrained at the contact points between the particles via Van der Waal and electrostatic forces with the container surfaces, hence supporting the bearing reaction forces at the extreme locations. The experimental data also indicate that the change in char weight after conversion during any experiments did not result in any substantial weight loss even when oxidant flow was maintained for a long period of time (see Fig. 12). Based on the numerical analyses presented above as also verified with experimental results, it is conjectured that nearly no particles escaped the char particle container during the experiments. To maintain equilibrium on the particle, the resultant forces required were 1.98e-26 N and 4.73E-22 N when considering the lift forces. However, the calculated anchoring force (3.75e-19 N) was much greater than these forces. Therefore, most of the weight losses measured during the experiments were attributed to the conversion of char to either CO or CO_2.

4.2 Experimental Setup and Procedure. Figure 4 shows the experimental char reduction setup used to perform the experiments using oxygen (O_2) as the oxidizing agent and hot vitiated air to preheat the reactor section at the desired temperatures. The reactor was slightly pressurized to reduce air infiltration into the system. The samples were lowered into the reaction zone when the temperature reached 100 °C to ensure that the experiments started only at dry state condition. The hot gas stream produced from the combustion of propane (C_3H_8) was used to preheat the reactor and also to provide the gasifying agents to central test section of the reactor at the desired temperature. For combustion, pure O_2 was injected at reactor temperature of 504, 584, and 644 °C. All sample char particles were contained in stainless steel pan as shown with approximately half of the char particle surface areas receiving direct interaction with the surrounding oxidant via diffusion through the stagnant layer. These temperatures are within the starting point of char combustion and gasification experiments [25–27]. The sample fine char particles were evenly spread out inside the reaction container to form a nearly uniform thin layer of particles of about 1.52 mm thickness to reduce the resistances due to internal diffusion. The applied heating rates during the preheat stage of char oxidation experiments was nearly identical

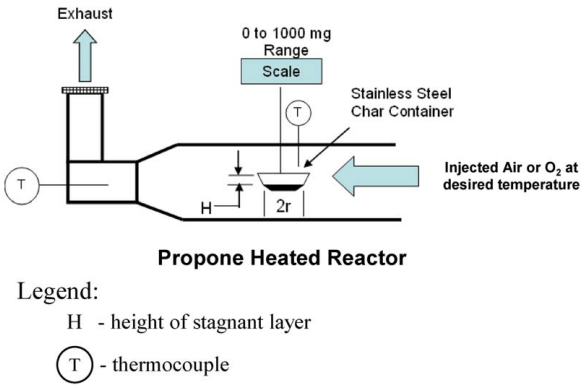

Fig. 4 Bench scale experimental facility

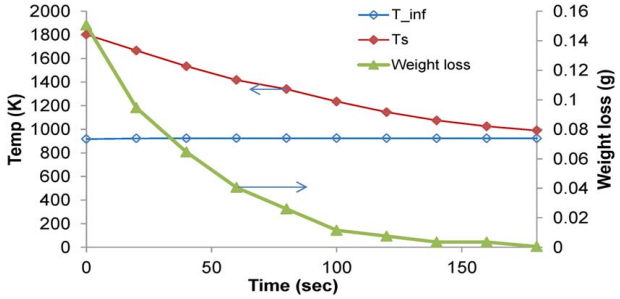

Fig. 5 Char surface temperature profile for 644 °C injection temperature

for all three (3) cases to ensure that the calculated kinetic parameters offer meaningful comparison under various oxidation conditions and reactor temperatures. The preheating stage was between room temperature and the predetermined injection temperatures for the three temperature cases examined here. Equilibrium calculations for the stoichiometric combustion of propane indicated that the gases used to heat up the reactor zone contained 0.9% argon, 0.1% CO, 8.4% CO_2, 11.3% H_2O, 5.4% O_2, and 73.4% N_2 on mole basis. Gas chromatographic analysis also indicated good similarity with the equilibrium values. The preheating rates for all the experiments were maintained between 118 and 120 °C/min.

The experiments were performed under identical conditions except for the injection temperatures, which were pre-selected from several preliminary tests, that allowed complete conversion of the char sample particles for each test. This allowed the use of lowest thermal energy input required to eliminate the char samples using pure oxygen as the oxidant. Three sample sizes of 0.2 g were examined at 4 flowrates with pure O_2 as the oxidant at various injection temperatures, ranging from 504 to 644 °C. Low or moderate temperature conditions were especially considered advantageous to ensure that the least amount of energy was expended for 100% conversion of the char. Besides calculating the intrinsic kinetic parameters, it was also important to know the efficiency or effectiveness of conversion. The energy requirements for each of these cases were also evaluated to determine the most efficient conditions for char oxidation in pure O_2.

5 Results

5.1 Effect of Injection Temperature on Char Surface Temperature. Figures 5–7 show the profiles of estimated char surface temperature as a function of reaction time for each of these cases. The char surface temperature is labeled as T_s and the reactor temperature is labeled as T_{inf}. Reactor temperatures were measured with a thermocouple located upstream of the sample location. Based on energy calculations, the energies released during the accelerated reactions were more likely due to $C + O_2 \rightarrow CO_2$

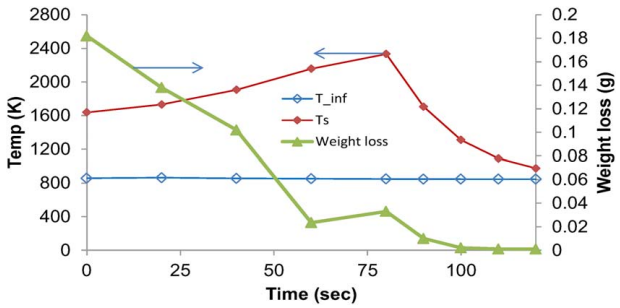

Fig. 6 Char surface temperature profile for 584 °C injection temperature

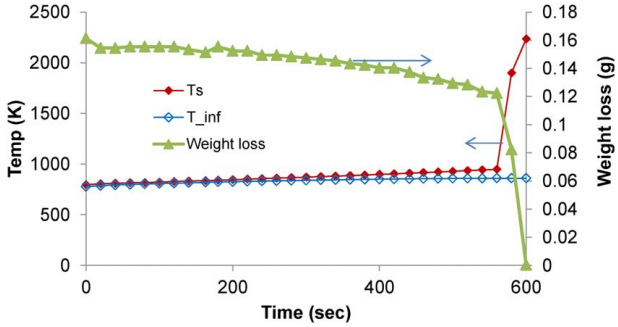

Fig. 7 Char surface temperature profile for 504 °C injection temperature

reaction. This was established by the fact that $C + O_2 \rightarrow CO_2$ reaction provided a better fit as compared with $C + ½\ O_2 \rightarrow CO$ reaction for all the cases. The estimated maximum char surface temperatures during the accelerated periods were 2333 ($t = 80$ s) and 1802 K ($t = 0$ s) for O_2 injection at temperatures of 584 and 644 °C, respectively.

At the lowest injection temperature of 504 °C, the estimated char surface temperature was 2235 K at 600 s at the end of the accelerated reduction period. This period corresponds to reactor temperature of 587 °C, which is very close to the other case with the injection temperature of 584 °C. This implies that the lowest temperature for $C + O_2 \rightarrow CO_2$ reaction will occur at reactor temperatures as low as 584 °C.

For injection temperatures at 584 and 644 °C, the surface temperatures were significantly higher than the reactor temperatures when the char conversion begins to accelerate. The char surface temperature with the highest injection temperature case of 644 °C began with the maximum char surface temperature of 1802 K and then decreased with conversion. The char surface temperature for the second case at 584 °C increased from 1600 K, reaching a maximum value of 2333 K. For the 504 °C case, the char surface temperature gradually increased and then rapidly increased when the reactor temperature reached 587 °C. The highest peak temperature for this case was 2235 K, which also matched the greatest char conversion rate (4.1E-03 g/s) when compared the other injection temperatures at 584 °C (6E-03 g/s) and 644 °C (3.5E-03 g/s). The estimated maximum temperatures were lower by some 100 to 400 °C as compared with the measured temperatures for the combustion of coal char particles under enriched oxygen environments that ranged between 2300 and 2400 K with very small coal particles of 106–125 μm [9]. This was expected because the coals used by Murphy and Shaddix [9] had high volatile matter (between 34 and 37%) as compared with carbon black particles used here which contained only about 0.1% tar. The trend for the weight

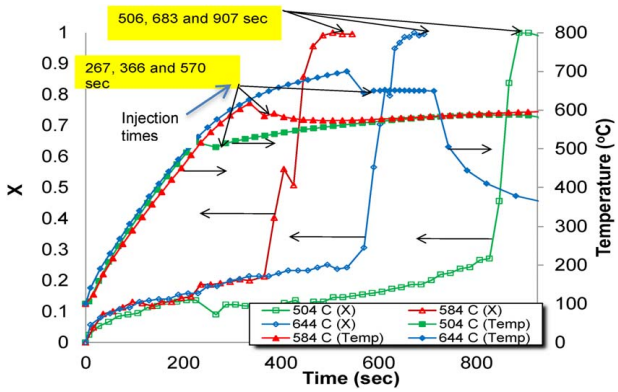

Fig. 8 Char conversion of 0.2 g sample with 4 m^3/h O_2

losses is also shown in these figures. For the injection temperatures at 644 and 584 °C, the weight decreased rapidly at the beginning that showed weight loss of 3.5E-03 and 2.6E-03 g/s, respectively. The rate of weight loss decreased with increase in reaction time for all the cases examined. However, for 504 °C, the highest weight loss rate occurred near the end of conversion at 4.1E-03 g/s (see Fig. 8).

The lowest injection temperature examined at 504 °C required the least amount of input energy to eliminate the same amount of char. However, the least amount of oxygen used for these cases was for injection temperature of 584 °C case. Preheating the reactor with vitiated air serves as a good practice to reduce input energy before injecting costly oxidants into the reactor.

5.2 Effect of Injection Temperature Using Pure Oxygen. Figure 8 shows the results obtained on the complete combustion of 0.2 g sample, using pure oxygen at a constant flowrate of 4 m^3/h and injection temperatures of 504 °C, 584 °C, and 644 °C. All the three cases reached 100% conversion with the subsequent release of energy from exothermic reactions. It took 640, 140, and 113 s to reach 100% conversion at injection temperatures of 504, 584, and 644 °C, respectively. A long induction period (560 s) had occurred for the lowest injection temperature of 504 °C This induction period is associated with the non-accelerated reduction condition from the time of injection to the time of accelerated reduction. However, the other higher injection temperatures (i.e., at 584 and 644 °C) exhibited no induction period, because the adsorption of O_2 gas within the particles occurred almost instantly when O_2 was injected into the reactor. This indicates that char reactions for injection temperatures at 584 and 644 °C occurred quickly as indicated by the estimated char surface temperatures of 1600 and 1800 K, respectively with O_2 injection. Based on the lowest injection temperature at 504 °C, the lowest reactor temperature at which the accelerated reduction starts to occur was 584 °C. When the reactor furnace was turned off to inject pure oxygen at these temperatures, the furnace temperature dropped for some period of time and then increased for all cases until most of the char was consumed. The reactor temperature operated nearly isothermally at the beginning of the accelerated conversion at 644 °C. This condition continued up to the time when the char particles were fully combusted. This implies that the heat release during char combustion was about equal to the heat loss by the furnace to its surroundings plus the heat loss due to convection of gas products to the exhaust system. However, for lower injection temperatures of 504 and 584 °C, reactor temperature increased and decreased, respectively for some time when the furnace was turned off. However, the reactor temperatures increased again. All char reductions were characterized as exothermic reactions, either due to $C + 1/2O_2 \rightarrow CO$ or $C + O_2 \rightarrow CO_2$ reaction. These reactions were observed by the slight increase in conversion for $T = 504$ °C from 10% at the beginning of injection up to 27%.

5.3 Effect of Air and Partial CO_2 Gasification Models at Preheat Stages. Two approaches were used here to model the char reduction during the preheating stages with the goal to examine:

- Compare the accuracy of these two models when reduction data are fitted into the model equation.
- Existence of apparent kinetic parameters.
- Determine and compare the predicted regimes for these two approaches.

In the first approach, the process was modeled using pure air as the gasifying agent. Stoichiometric coefficient values of 1.33 and 2.66 were used in the ash segregated core model (ASCM) equation to verify which of these two values provide a better fit to the experimental values. Based on this numerical test, it was determined that a stoichiometric coefficient (v_I or v) value of 1.33 fitted better with the experimental data as compared with 2.66 value. This suggests

that the char reduction at the preheating stages is mainly caused by air gasification. This model was first applied to determine the effects of external or surface chemical reactions and diffusion. However, it was determined that the weight loss was attributed to only pure diffusion and that no external chemical reactions existed.

Because the model for char reduction behavior during the preheating period was not a robust fit in the first modeling case, a second model was also investigated by using partial CO_2 gasification. This model coupled the diffusion and kinetic effects during the preheating stages up to the time of oxidant injections at the predetermined injection temperatures. This model assumed that both diffusion and kinetic effects were important during the preheating stage. Because the CO_2 component has highest mass fraction (~16% based on equilibrium calculations) for vitiated air, the preheating stage was modeled as a partial CO_2 gasification condition. This was accomplished by treating the mass fractions of H_2O (~9%) and O_2 (~2.6%), both based on equilibrium calculations and CO_2 mass fractions to account for the gasifying agents (H_2O and O_2). Although this was not the actual case, this model reduced mathematical complexity associated with multi-component diffusion coefficients and reactions.

Figures 9–11 provide a visual representation of the air gasification model (with first modeling case labeled in the plots is "diffusion controlled") for the three temperature cases. Figures 12–14 provide the effect of partial CO_2 gasification model (second modeling case, labeled in the plots as "simulated CO_2 gasification") for the three temperatures cases examined. These clearly reveal that simulated partial CO_2 gasification model provides a closer fit as compared with air gasification for the preheating stages with vitiated air. An evaluation of the standard deviations for the two models as compared with the experimental data is provided. The calculated KPs for these two models are also presented in Sec. 5.4.3.

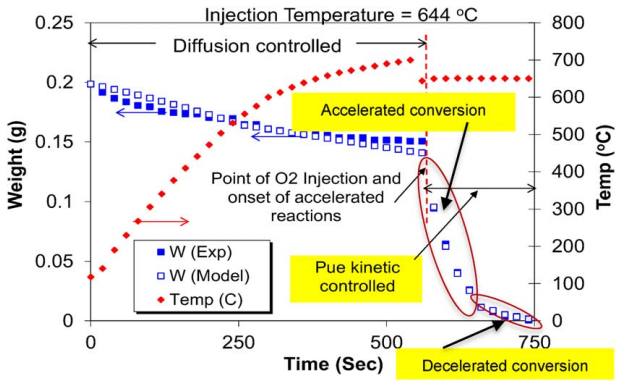

Fig. 9 Modeling weight loss for 0.2 g char with O_2 oxidation at $T_0 = 644$ °C using DNLF model

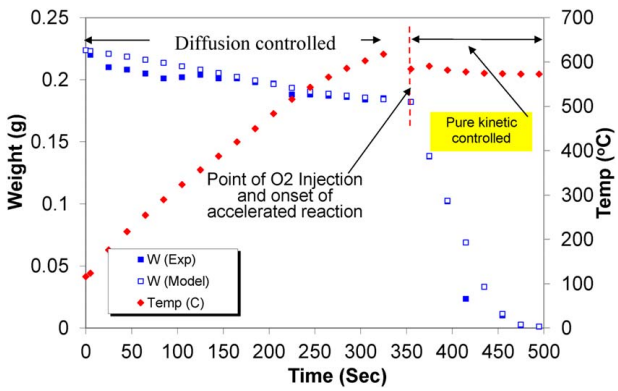

Fig. 10 Modeling weight loss for 0.2 g char with O_2 oxidation at $T_0 = 584.6$ °C using DNLF model

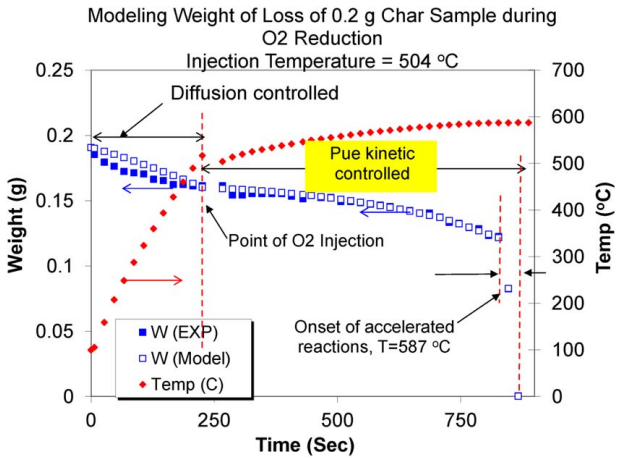

Fig. 11 Modeling weight loss for 0.2 g char sample during char reduction at $T_0 = 504$ °C using DNLF model

5.4 Effect of Temperature for Calculating the Kinetic Parameters in Simulated Gasification and Combustion. The two modeling approaches were also used to model the char reduction with O_2 injection in the combustion period via the one-film ASCM. The main objectives were to determine:

- Intrinsic kinetic parameters and dominant regimes.
- Effect of using discrete time linear and nonlinear fits to the Arrhenius equation in calculating the kinetic parameters.

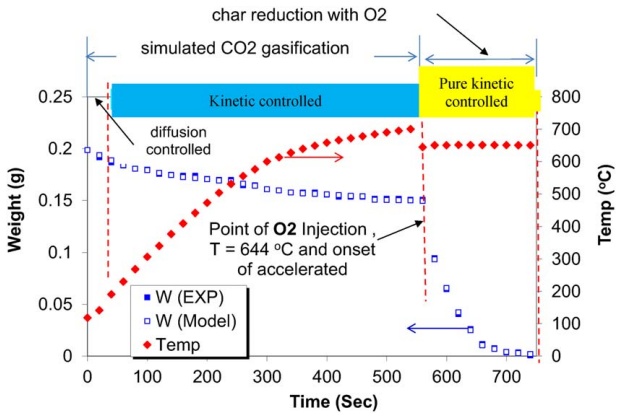

Fig. 12 Modeling weight loss for 0.2 g char at $T_0 = 644$ °C with DLF model

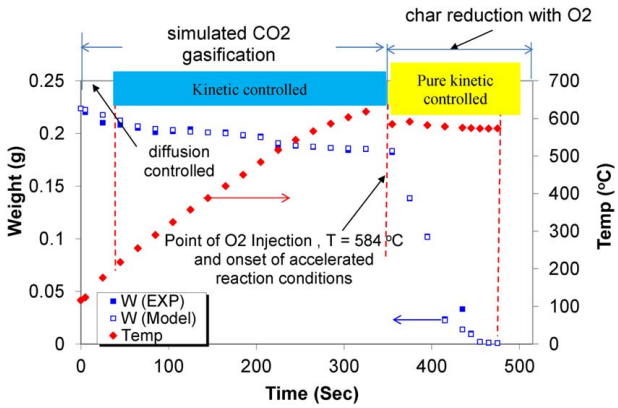

Fig. 13 Modeling weight loss for 0.2 g char at $T_0 = 584$ °C with DLF model

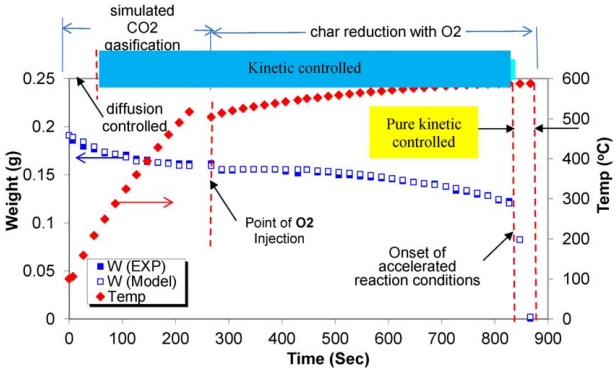

Fig. 14 Modeling weight loss for 0.2 g char at $T_0 = 504$ °C with DLF model

- Effect of using temperatures as the basis for calculating the kinetic parameters.

The second portion of the reduction process ($C + O_2 \rightarrow CO_2$) was modeled as a purely kinetic-controlled process since this provided a good fit with the experimental data at injection temperatures of 504, 584, and 644 °C (see Figs. 9–11). For the lowest temperature case of 504 °C, the non-accelerated reaction region (from $t = 267$ to $t = 827$ s, in Fig. 11) was also modeled as pure kinetic control (no diffusion effects) because of good fit with the experimental data. To determine the regime of reduction, the mass fraction of oxygen ($Y_{O2,s}$) at the char surface was assigned as 100% at the beginning of the injection period and the diffusional effects were not considered in the ASCM equation to determine which fitted better for the different reduction temperatures examined. When the diffusional resistance effects were removed, the model fitted well with the experimental data, implying a pure kinetic-controlled condition when pure O_2 was injected. During this condition, a stoichiometric coefficient value of 2.66 provided a good fit for all test cases examined as compared with coefficient value of 1.33. This suggests that the second portion of the reduction period was also dominated by $C + O_2 \rightarrow CO_2$ reaction. This condition was determined to be the major reaction pathway for all cases during the non-accelerated, accelerated, and decelerated reduction/reaction conditions. There were no decelerated conditions for the lowest injection temperature of 504 °C. Nonetheless, this supports the concept that particles tend to be dominated more by $C + O_2 \rightarrow CO_2$ versus $C + ½\ O_2 \rightarrow CO$, which occurs very close to the external surface of spherical particles with particle disk diameters greater than 1.5 mm [8]. With oxygen injection, we assumed that the vitiated air quickly purged out with the pure oxygen. Numerical analysis also supported pure kinetic-controlled regime at the char surface. Mathematically, this was applied by assigning unity oxygen mass fraction at the char surface. The diffusion term contribution in Eq. (7) was treated as zero because this occurred infinitely fast. Because the char surface temperatures were not known, the observed reactor temperatures were used to calculate the kinetic parameters. After O_2 injection, the surface oxygen mass fractions were modeled as unity or 100%.

The second case used had a more rigorous approach that supported as an alternative to the first modeling approach. This modeling case explored the effects of both diffusion and kinetics for entirety of the char reduction, starting with the preheating stage using vitiated air up to the time of pure O_2 injection. This procedure was also expected to provide unique values of activation energies and frequency factors when using a discrete linear fit (DLF) approach to calculate the Arrhenius parameters at the preheat, non-accelerated, accelerated, and decelerated regions.

5.4.1 Discrete Nonlinear Fit Modeling Results Using T_∞. For DNLF, the calculated activation energy for the accelerated region was 126 kJ/mol with a trial frequency factor of 1.0E+06 m/s at 644 °C. This trial frequency factor was also applied to all the other cases examined. Ultimately, the frequency factor values were refined using DLF method on the Arrhenius equation. For the same temperature (644 °C), under the decelerated regions, the nonlinear fit was also used to calculate the activation energies and these were found to vary between 138 and 140 kJ/mol, which indicates decreased reactive condition as compared with the case with activation energy value of 126 kJ/mol. This is attributed to ash layer that blocks the penetration of O_2 gas into the particle surface (see Fig. 4). Note that the reactor temperatures were nearly isothermal at around 650 °C (see Fig. 9).

The same modeling approach was used for the second sample test case at $T = 584$ °C (see Fig. 10), with diffusion-controlled air gasification used for the preheat stage and pure kinetic controlled for the reaction stage. For nonlinear fit method, the calculated activation energy values varied between 117 to 120 kJ/mol and 119 to 137 kJ/mol with a frequency factor of 1.00E+06 m/s during the accelerated and decelerated periods, respectively. As observed earlier with the first test case at 644 °C injection temperature, the activation energy increased during the deceleration period with an average value of 9.5 kJ/mol, which indicates decreased reactive surface due to the inhibiting effects of ash formation.

In contrast to the previous two cases, the third test case (at $T = 504$ °C) provided a non-accelerated period after O_2 injection. This period occurred for 560 s before the weight loss rate accelerated (see Fig. 11). The estimated activation energies at discrete period for the non-accelerated region was 144 kJ/mol. However, for the accelerated region, the activation energies varied between 110 and 141 kJ/mol. Similar to the previous two cases, this indicates that non-accelerated period was less reactive as compared with the accelerated condition because of higher value of activation energy.

Figure 11 shows the modeling results with the lowest injection temperature of 504 °C using the same mass of char (0.2 g) and O_2 flowrate. As compared with the injection temperatures at 644 and 584.6 °C, the reaction at 504 °C took considerably long time (600 s) to completely eliminate the char.

The two regions indicate the two possible types of dominant reactions. The first one is called the non-accelerated region, which seems to be dominated by $C + 1/2O_2 \rightarrow CO$ mechanism. However, when this was tested and verified using Eq. (7) by checking the governing stoichiometric coefficients, the $C + O_2 \rightarrow CO_2$ model provided a better fit as compared with the gasification reaction. Similarly, the accelerated region was dominated by $C + O_2 \rightarrow CO_2$ because this also fitted well with the experimental data. Equation (7) suggests that the accelerated region was purely combustion and kinetically controlled.

All the calculations were based on a constant frequency factor using a nonlinear approach for the reactor temperatures. Because of the variability of activation energies with respect to the order of reaction, the kinetic parameter calculations were not unique and highly likely not a good representation of their actual values [16]. It was also found that an increase in frequency factor also caused an increase in calculated activation energy values. Therefore, the kinetic parameter calculations could vary and it is recommended that further investigations should be performed using discrete linear fit approach while also using the estimated char surface temperatures for kinetic calculations instead of the reactor temperatures used here.

5.4.2 Discrete Linear Fit via T_s and CO_2 Gasification Model. CO_2 gasification is important that help assists with the CO_2 utilization. The DLF model was applied for preheat stages to determine if the model fidelity could be improved from the air gasification case. Also, instead of using the reactor temperatures (First model case) via DNLF, the char surface temperature (Second model case) was used to calculate the kinetic parameters with DLF from the Arrhenius equation during the oxidation stages for all cases. For the first test case (at $T = 644$ °C), the DLF provided a pure diffusion-controlled regime for the first 60 s during the preheat stage

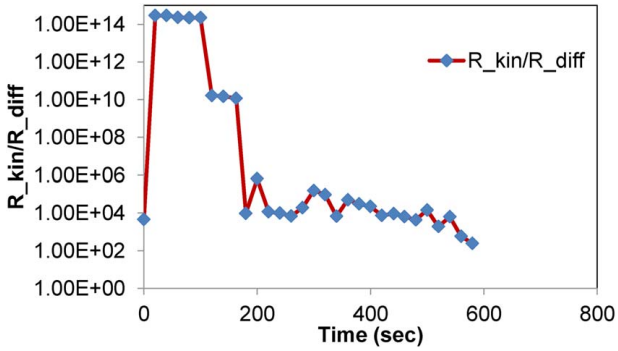

Fig. 15 Ratio of R_{kin}/R_{diff} during the non-accelerated region for $T_0 = 504$ °C

(see Fig. 12). As the temperature continued to increase beyond 60 s, the regime was characterized as kinetic-controlled. However, numerically, diffusion effects were observed important during this heating period. Subsequently, when pure O_2 was injected at 644 °C, an intrinsic kinetic-controlled condition was observed during the entire period, showing two trends of accelerated reduction for the first 80 s and a deceleration reduction that lasted for about 20 s toward the end (see Fig. 12) labeled as "char reduction with O_2." Overall, this case revealed that a pure or intrinsic kinetic-controlled process existed for the accelerated and decelerated regions.

For the second modeling approach, it was also observed that CO_2 gasification model fitted better with the data as compared with air gasification case during the preheat stage (see Fig. 13). Similar to the first test case, the second test case at $T = 584$ °C injection temperature provided pure diffusion-controlled regime for the first 60 s during the preheat stage. Beyond the first 60 s, as the temperatures continued to increase until reaching the injection temperature and the regime were characterized as pure kinetic-controlled. Note that the diffusion effects were also observed to be important during the heating up period. However, when pure O_2 was injected at 584 °C, a pure or intrinsic kinetic-controlled model existed during the entire char reduction period, showing two trends of an accelerated reaction process for the first 60 s from the point of O_2 injection and a deceleration reaction process that lasted about 60 s toward the end.

For the lowest injection temperature case at 504 °C, it was further observed that CO_2 gasification model provided better fit when compared with the air gasification model during the preheat stage (see Fig. 14). Similar to the previous two test cases, this test case provided pure diffusion-controlled regime for the first 60 s. Beyond the first 60 s, as the temperatures continued to increase until reaching the injection temperature, the regime was characterized as kinetic-controlled. However, diffusion effects were also observed to be important during this heating period. When pure O_2 was injected at 504 °C, a diffusion-kinetic-controlled model was observed during the non-accelerated reduction period. Overall, the combustion reduction process showed two trends of kinetic-controlled process and an accelerated reduction process that lasted for about 40 s toward the end. The diffusion-kinetic-controlled process at the non-accelerated region appeared to be controlled by chemical reactions (i.e., the ratio of R_{kin} to $R_{diff} > 1$), especially at the beginning for at least the first 180 s in the non-accelerated region (see Fig. 15). Overall, it was observed that a pure kinetic-controlled process existed for this case but only during the accelerated region.

5.4.3 Estimated Kinetic Parameters. Table 2 provides a summary of the kinetic parameters for all the modeling results at the specified discrete regions, which include the heating periods, non-accelerated, accelerated and decelerated conditions. As expected, the heating periods were endothermic, while the rest of the conditions were exothermic. The char surface temperatures were calculated based on the energy equations presented earlier. IT, TR, Ts, and NC are acronyms for injection temperature, reactor temperature, char surface temperature and "not calculated", respectively. Discrete time nonlinear fit method was used to evaluate the Arrhenius equation at various regions for the first model case. Pure air gasification reductions were also applied for the first model case, which provided pure diffusion (no kinetic reduction effects) during the preheat stage. This first model case also calculated the kinetic parameters based on reactor temperatures and it showed that during char combustion (i.e., non-accelerated linear, accelerated, and decelerated region), there was an increase in the activation energy from the accelerated region to the decelerated region. Table 2 shows a decrease in activation energy (from 144 to 124 kJ/mol) from the non-accelerated region to the accelerated region for the 504 °C injection temperature. A constant frequency factor of 1.0 E+06 m/s was used for the first model case.

Discrete linear fit on the Arrhenius equation was used for the second model case, starting at the preheat stage, which was modeled as CO_2 partial gasification. The increase in activation energy (37.3–69.5 kJ/mol) was observed with the second model case at 644 °C progressing from the accelerated region to decelerated region. Based on the first and second model cases, the

Table 2 Modeling results for the KPs for various injection temperatures (IT)

							First model case		Second model case	
IT (°C)	IT (K)	TR_{min} (K)	TR_{max} (K)	Ts_{min} (K)	Ts_{ave} (K)	Ts_{max} (K)	E_a (kJ/mol)	A (m/s)	E_a (kJ/mol)	A (m/s)
Heating period (modeled as air and CO_2 gasification for 1st and 2nd case models, respectively)										
644	917	391	968	298	723	952	NC	NC	NC	NC
584	857	389	876	298	574	845	NC	NC	29.0	9.72E+02
504	777	373	790	298	495	743	NC	NC	21.9	2.57E+02
Non-accelerated (linear) region with O_2										
504	777	777	860.2	796	869	942	144	1.00E+06	108.8	3.62E+06
Accelerated region with O_2										
644	917	917	923	1235	1552	1802	126	1.00E+06	37.3	1.86E+03
584	857	850	860	1637	1953	2333	119	1.00E+06	94.9	5.53E+04
504	777	777	860.2	949	2067	2235	124	1.00E+06	NC	NC
Decelerated region with O_2										
644	917	920	920	990	1093.6	1145	139	1.00E+06	69.5	2.20E+04
584	857	850	850	973	1270.6	1705	128	1.00E+06	52.6	5.40E+03
504	777	860	860	NC	NC	NC	NC	NC	NC	NC

Note: NC, not calculated; IT, injection temperature; *TR*, temperature of reactor; and *Ts*, surface temperature.

Table 3 Overall modeling results during reduction

E_a (kJ/mol)	IT (°C)	A (m/s)	$T_{s,ave}$ (K)	$\dot{m}_{ave}$	W_{ash}/W_{carbon}
50.2	584	3.5E+04	1649.7	1.51E-06	2.9
67.5	644	3.7E+03	1322.9	9.3E-07	2.4
74.9	504	1.9E+04	946.1	3.3E-07	0.7

Note: IT, injection temperature; $T_{s,ave}$, average surface temperature; and W, weight.

activation energies were strongly influenced by char surface temperatures. For initial temp (IT) of 644 °C, the activation energy decreased from 126 kJ/mol (first model case) to 37.3 kJ/mol (second model case) during the accelerated region. The decelerated reaction period also provided lower activation energy and frequency factor of 69.5 kJ/mol and 2.2 E+04 m/s, respectively, for the second model case as compared with the first model case that provided values of 139 kJ/mol and 1.0 E+06 m/s.

The results obtained on kinetic parameters, char surface temperatures, char burning rates ($\dot{m}$), and ash contents are provided in Table 3 for the overall reduction or combustion (non-accelerated, accelerated, and decelerated regions) of flat thin-shaped char particles. These data were obtained using the second model case. The results show that higher average values of char surface temperatures, char burning rates, and ash contents resulted in lower activation energy and frequency factor. These results indicate that the combustion of these particles was purely (intrinsic) kinetic controlled as indicated by using char reduction model equations for flat thin-shaped particles (presented earlier).

5.5 Energy Released for Each Case Based on Different Injection Temperatures. Table 4 shows the total energy released per weight converted and also the peak energy released. Among the three cases investigated, the highest total energy released was 40.6 kJ/g when combusting char with O_2 at 584 °C. However, this case (No. 2) provided the least peak energy released at 85.3 J/s. This shows that injection temperatures play an important role on the energy released and peak energy during combustion. System thermal efficiencies were also calculated for each case and case No. 3 provided the highest thermal efficiency primarily because this had the lowest operating injection temperature.

6 Comparison With the Literature

At the lowest injection temperature of 504 °C, the estimated maximum char surface temperature was 2235 K during the accelerated reduction period. The highest char surface temperature from this study was 2333 K, which is very close to measured temperatures of 2300–2400 K for the combustion of coal char particles under high enriched oxygen environments [7].

Table 5 provides a comparison of obtained combustion kinetic parameters for the flat-shaped chars examined here along with a very similar study reported in the literature [25]. As discussed earlier, the flat thin char particles operated under pure kinetic control conditions during the reduction stage. The activation energy values varied between 50 and 74.9 kJ/mol (see item 5 in Table 5), which are comparable with those obtained (see item 4 in Table 5 with activation energy values between 40 with 78.6 kJ/mol)

Table 4 Peak and total energy release

Case Nos.	Model shape	Initial weight (g)	No. of sample pieces	O_2 flow (m^3/h)	IT (°C)	Peak energy released (J/s)	Total energy released (kJ/g)	E_a (kJ/mol)	A (m/s)	$T_{s,ave}$ (K)	Thermal efficiency (%)	X_{max}
1	Flat disk	0.151	1	4	644	116.0	33.0	74.9	3.5E+04	1322.9	0.1249	1.0
2	Flat disk	0.182	1	4	584	85.3	40.6	50.2	3.7E+03	1649.7	0.2959	1.0
3	Flat disk	0.161	1	4	504	134.5	32.8	67.5	1.9E+04	946.1	0.3143	1.0

Note: IT, injection temperature.

Table 5 Kinetic parameters summary along with the reported values from the literature

Item Nos.	Model shape	Oxidant	t (mm)× d (mm) × H (mm)	Ts (K)	E_a (kJ/mol)	A, ASCM (m/s)	A, Arrhenius type (1/Pa s)	Method	X_{max}	$\dot{m}_{ave}$ (g/s)	Porosity (%)	R_{kin}/R_{diff}	Processing rate (g/h)	References
1	Flat disk	Air	1.23 × 4 × 3	848–923	124		1.64E+01	Arrhenius type	0.6	3.00E-06		Very large	0.011	[17]
2	Flat disk	Air	1.23 × 4 × 3	1264–1375	89.5	2.49E+07		One-film model (this study)	0.6	3.00E-06		Very large	0.011	[17]
3	Flat disk	Air	1.23 × 4 × 3	923	125.0	5.00E+09		One-film model (this study)	0.6	3.00E-06		Very large	0.011	[17]
4	Flat disk	O_2	1.52 × 22.5 × 25	946–1650	40–78.6		6.1E-06–8.4E-05	Arrhenius type	1	9.22E-04	83	Very large	3.3	This study
5	Flat disk	O_2	1.52 × 22.5 × 25	946–1650	50.2–74.9	3.72E+03–3.50E+04		One-film model (this study)	1	9.22E-04	83	Very large	3.3	This study

Note: t, thickness; d, diameter; H, height of stagnant layer; E_a, activation energy; A, frequency factors; X_{max}, maximum conversion; Ts, char surface temperature; $\dot{m}_{ave}$, average burning rate; and R_{kin}/R_{diff}, ratio of resistances of kinetic rates to diffusion rates.

using Arrhenius type equation [25]. Note that the activation energy values are influenced by the type of oxidants used. Combustion of char particles with pure O_2 provided more reactive conditions as supported from the much lower values of activation energy (i.e., values between 50.2 and 74.9 kJ/mol) versus pure air case (124 kJ/mol using Arrhenius type model or 125 kJ/mol when using the one-film model (Eq. (3)). The Arrhenius type model presupposes that the regime of reduction is intrinsic, which is ideal for tiny particles. The one-film model used to calculate the kinetic parameters of Jaramillo et al. [25] data provided the activation energy value of 89.5 kJ/mol when char surface temperatures were considered. This value was expected to be lower than those obtained in this investigation because pure O_2 as oxidant provides a more reactive condition than air. Based on a unity order of reaction with a frequency factor constrained at 1.0 E + 06 m/s, the activation energies for all cases using discrete time nonlinear approach varied between 119 and 126 kJ/mol (see Table 2). These values are estimated based on the accelerated reduction regimes, which are close to those obtained by Jaramillo et al. for carbon black [25]. This was expected because the activation energy calculations by Jaramillo et al. were based on the reactor temperatures.

The heating value of solid fuels was approximated using the Dulong's empirical formula [28] in the form:

$$\text{HHV} = 33.96\,\text{C} + 141.890(\text{H} - \text{O}/8) + 9.42\,\text{S}\ \text{kJ/g} \qquad (15)$$

where C, H, O, and S are the weight fractions of carbon, hydrogen, oxygen, and sulfur for solid fuels. For all cases in this study, the total energy released per unit weight converted varied between 32.8 and 40.6 kJ/g. These values do not agree well with Dulong's empirical formula. This is expected because Dulong's empirical equation typically does not do well at predicting the heating values of some solid fuels, especially biomass [29].

7 Conclusions

Flat thin chars with maximum thickness of up to 1.52 mm was examined as it reacted with 100% O_2. Char and O_2 reactions showed that these were mostly intrinsic kinetic-controlled conditions during the conversion process. The one-film model used here demonstrated that intrinsic kinetic parameters can be characterized via discrete time nonlinear and linear fits to the Arrhenius equation. However, discrete time nonlinear method can only be applied when the frequency factors are known. Nevertheless, this method provided a relative measure of reactivity of char reductions to conclude:

- At the lowest injection temperature of 504 °C, the induction period was long, which was associated with the non-accelerated reduction condition during O_2 injection. However, the other higher injection temperatures exhibited no induction period, which indicated the full adsorption of O_2 gas within the particles to occur almost instantly during O_2 injection. This also indicates that reactions for injection temperatures at 584 and 644 °C occurred quickly as indicated by the estimated maximum char surface temperatures of 2333 and 1802 K, respectively, when O_2 was injected.
- At the lowest injection temperature at 504 °C, the estimated maximum char surface temperature was 2235 K during the accelerated reduction period. This period corresponds to the measured reactor temperature of 587 °C, which is very close to the other case with injection temperature of 584 °C. This suggests that lowest operating reactor temperature for char with O_2 can occur instantly at reactor temperatures as low as 584 °C.
- The highest char surface temperature from this study was 2333 K, which was close to measured temperatures from the combustion of coal char particles under high enriched oxygen environments (reported in the range of 2300–2400 K [9]).
- Partial CO_2 gasification model provided a closer fit to the experimental data as compared with pure air gasification case for the preheat periods with vitiated air for all the injection temperature cases examined.
- A stoichiometric coefficient value of 2.66 provided a better model fit to experimental data as compared with 1.33 for all the test cases. This suggests that the second portion (combustion condition) of the reduction period was dominated by $C + O_2 \rightarrow CO_2$ reaction. This condition was determined to be the major reaction pathway during the non-accelerated, accelerated, and decelerated reduction conditions. This also supports the claims of some authors that particles tend to be dominated more by $C + O_2 \rightarrow CO_2$ instead of $C + O_2 \rightarrow CO$ [8].
- Based on the unity order of reaction with a frequency factor constrained at 1.0 E+06 m/s, the activation energy for all cases using discrete time nonlinear approach varied between 119 and 126 kJ/mol. These values were estimated based on the accelerated reduction regimes, which are close to those obtained by Jaramillo et al. for carbon black [25]. This was expected because the activation energy calculations by Jaramillo et al. were based on the reactor temperatures.
- The decrease in value of both activation energy and frequency factor with the second CO_2 modeling case was influenced by higher values of the rate of change of mass ($\dot{m}$, g/s), average char surface temperatures, and ash content during conversion.
- In modeling char reductions, fitting the data allows one to determine the regime of char reduction and the kinetic parameters. When the diffusion contribution was not considered, a good fit could be obtained, allowing one to determine that a pure kinetic process or pure Zone I combustion existed. This suggests that the estimated kinetic parameters are intrinsic. Conversely, during the preheat periods with the use of vitiated air model, when the kinetic contribution was not included in the model, the data fitted well. This suggests that the operational regime was purely under diffusion conditions (pure Zone III), i.e., R_{kin}/R_{diff} equals zero.
- The one-film model successfully provided energy parameters and characterized the regimes of preheat, gasification, and combustion.
- Successfully demonstrated the shrinking model used for the reduction on char radius during combustion and gasification.

Acknowledgment

The authors acknowledge the financial support provided by the Office of Naval Research, Program Manager Dr. Steve McElvany. The technical assistance provided by Ms. Danica Gordon and Ms. Rachel Kang on this project at the University of Maryland Combustion laboratory is also very much appreciated.

Conflict of Interest

There are no conflicts of interest.

Data Availability Statement

The datasets generated and supporting the findings of this article are obtainable from the corresponding author upon reasonable request. The authors attest that all data for this study are included in the paper. Data provided by a third party listed in Acknowledgment. No data, models, or code were generated or used for this paper.

Nomenclature

m = mass of char
n = order of reaction in O_2
r = initial radius of the char in the container

t = time of conversion, s
A = pre-exponential factor, m/s
D = diffusivity
H = height of the stagnant layer
N = number of syngas species
R = universal gas constant
T = temperature of interest, K
$[i]$ = molar concentration of species "i"
v_I = one-film stoichiometric coefficient
E_a = activation energy, kJ/mol
dt = time-step
k_j or k_c = rate coefficient of reaction "j" or reaction rate constant
C or $C(s)$ = char or carbon
MW_{mix} = molecular weight of gas mixtures
MW_j = molecular weight of gas species
Yi,s = mass fraction of species "i" at the surface
Yi,∞ = mass fraction of species "i" at far field

Subscripts

a = activation
i or j = species (reactants or products) or reactions
s = surface location
∞ or inf = far field location

References

[1] Laohalidanond, K., Kerdsuwan, S., Burra, K. G., Li, J., and Gupta, A. K., 2021, "Syngas Generation From Landfills Derived Torrefied Refuse Fuel Using a Downdraft Gasifier," ASME J. Energy Resour. Technol., **143**(5), p. 052102.
[2] Kerdsuwan, S., Laohalidanond, K., and Gupta, A. K., 2021, "Upgrading of Refuse Derived Fuel Properties From Reclaimed Landfill Using Torrefaction," ASME J. Energy Resour. Technol., **143**(2), p. 021302.
[3] Wang, Z., Burra, K. G., Liu, X., Li, X., Zhang, M., Lei, T., and Gupta, A. K., 2021, "Synergistic Effect on CO_2 Assisted Gasification of Biomass and Plastics," ASME J. Energy Resour. Technol., **143**(3), p. 031901.
[4] Scenna, R., and Gupta, A. K., 2018, "The Influence of the Distributed Reaction Regime on Fuel Reforming Conditions," ASME J. Energy Resour. Technol., **140**(12), p. 122002.
[5] Trehan, K., Molintas, H., and Gupta, A. K., 2014, "Gasification of Torrefied and Soft Wood Pellets in Air and CO_2," ASME Power Conference, Baltimore, MD, July 28, Paper No. Power 2014-32230.
[6] Bai, Z., Wang, Z., Yu, G., Yang, Y., and Metghalchi, H., 2019, "Experimental Study of Laminar Burning Speed for Premixed Biomass/Air Flame," ASME J. Energy Resour. Technol., **141**(2), p. 022206.
[7] Yin, Y., Yin, J., Zhang, W., Tian, H., Hu, Z., Ruan, M., Song, Z., and Liu, L., 2018, "Effect of Char Structure Evolution During Pyrolysis on Combustion Characteristics and Kinetics of Waste Biomass," ASME J. Energy Resour. Technol., **140**(7), p. 072203.
[8] Dennis, J. S., Hayhurst, A. N., and Scott, S. A., 2006, "The Combustion of Particles of Char in Bubbling Fluidized Beds: The Dependence of Sherwood Number and the Rate of Burning on Particle Diameter," Combust. Flame, **147**(3), pp. 185–194.
[9] Murphy, J. J., and Shaddix, C. R., 2006, "Combustion Kinetics of Coal Chars in Oxygen-Enriched Environments," Combust. Flame, **144**(4), pp. 710–729.
[10] Molintas, H., and Gupta, A. K., 2011, "Kinetics of Char Reduction of Residual Char Particles Using Air and O_2," Appl. Energy J., **88**(1), pp. 306–315.
[11] Müller, R., Zedtwitz, P., Wokaun, A., and Steinfeld, A., 2003, "Kinetic Investigation on Steam Gasification of Charcoal Under Direct High-Flux Irradiation," Chem. Eng. Sci., **58**(22), pp. 5111–5119.
[12] Paviet, F., Bals, O., and Antonini, G., 2007, "Kinetic Study of Various Chars Steam Gasification," Int. J. Chem. React. Eng., **5**(1), p. Article No. A80.
[13] Backreedy, R. I., Fletcher, L. M., Jones, J. M., Ma, L., Pourkashanian, M., and Williams, A., 2005, "Co-Firing Pulverized Coal and Biomass: A Modeling Approach," Proc. Combust. Inst., **30**(2), pp. 2955–2964.
[14] Gera, D., Mathur, M. P., Freeman, M. C., and Robinson, A., 2002, "Effect of Aspect Ratio of Biomass Particles on Carbon Burnout in a Utility Boiler," Energy Fuels, **16**(6), pp. 1523–1532.
[15] Kajitani, S., Suzuki, N., Ashizama, M., and Hara, S., 2006, "CO_2 Gasification Rate Analysis of Coal Char in Entrained Flow Coal Gasifier," Fuel, **85**(2), pp. 163–169.
[16] Meng, X., Rokni, E., Zhou, W., Qi, H., Sun, R., and Levendis, Y., 2020, "Emissions From Oxy-Combustion of Raw and Torrefied Biomass," ASME J. Energy Resour. Technol., **142**(12), p. 122307.
[17] Gardiner, W. C., 1972, *Rates and Mechanisms of Chemical Reactions*, Benjamin Benjamin-Cummins Publishing Co., Menlo Park, CA, p. 284.
[18] Turns, S. R., 2000, *An Introduction to Combustion*, 2nd ed., McGraw Hill Book Co., pp. 656–658.
[19] Su, J. L., and Perlmutter, D. D., 1985, "Effect of Pore Structure on Char Oxidation Kinetics," AIChE J., **31**(6), pp. 973–981.
[20] Hong, L., and Luthy, R., 2007, "Availability of Polycyclic Aromatic Hydrocarbons From Lampblack-Impacted Soils at Former Oil-Gas Plant Sites in California, USA," Environ. Toxicol. Chem., **26**(3), pp. 394–405.
[21] Hong, L., Ghosh, U., Mahajan, T., Zare, R., and Luthy, R., 2003, "PAH Sorption Mechanism and Partitioning Behavior in Lampblack-Impacted Soils From Former Oil-Gas Plant Sites," Environ. Sci. Technol., **37**(16), pp. 3625–3634.
[22] Lide, D. R., 2005, *Handbook of Chemistry and Physics*, CRC Press, Boca Raton, FL, pp. 229–233.
[23] Leighton, D., and Acrivos, A., 1985, "The Lift on a Small Sphere Touching a Plane in the Presence of a Simple Shear Flow," J. Appl. Math. Phys., **36**(1), pp. 174–178.
[24] Stempniewicz, M. M., Komen, E. M. J., and de With, A., 2008, "Model of Particle Resuspension in Turbulent Flows," Nucl. Eng. Des., **238**(11), pp. 2943–2959.
[25] Jaramillo, I. C., Levinthal, J., Lighty, J. S., Gaddam, C. K., and Vander Wal, R., 2013, "Oxidation Kinetics and Nanostructure of Model Carbons Based on TGA Data," 8th Western States Section of the Combustion Institute U.S. National Combustion Meeting, May, pp. 1555–1564.
[26] Ahmed, I., and Gupta, A. K., 2009, "Syngas Yield During Pyrolysis and Steam Gasification of Paper," Appl. Energy, **86**(9), pp. 1813–1821.
[27] Ahmed, I., and Gupta, A. K., 2009, "Evolution of Syngas From Cardboard Gasification," Appl. Energy, **86**(9), pp. 1732–1740.
[28] Keating, E. L., 2007, *Applied Combustion*, CRC Press, Boca Raton, FL, p. 206.
[29] Jenkins, B. M., Baxter, L. L., Miles, T. R., Jr., and Miles, T. R., 1998, "Combustion Properties of Biomass," Fuel Process. Technol., **54**(1–3), pp. 17–46.